Efficient three-dimensional Laplace-Fourier domain acoustic wave simulations using discontinuous finite-difference meshes with embedded boundaries

Hussain AlSalem∗, *University of California at Berkeley*, Petr Petrov∗ and Gregory Newman, *Lawrence Berkeley Lab*, and James Rector, *University of California at Berkeley*

SUMMARY

We develop embedded boundary and discontinuous mesh methods to handle arbirarily shaped topography and accurately simulate acoustic seismic wave propagation in Laplace-Fourier domain. The purpose of the embedded boundary method is to enhance accurate wave simulation near the surface and the discontinuous mesh method is used to achieve considerable savings in both computation time and memory savings relative to fixed mesh schemes.

FINITE DIFFERENCE MODELING

Introduction

In acoustic seismic modeling, the objective is to describe the propagation of waves through the earth. Here, we consider wave propagation that is solved in the Laplace-Fourier Domain. We start by discretizing the three-dimensional wave equation on a Cartesian grid $x_{i,j,k} = (ih, jh, kh)$ in space, where $h > 0$ is the grid size. We let the Laplace frequency be complex-valued, $s = \sigma + i\omega$, consisting of a Laplace damping factor σ and the angular frequency ω. The solution to the forward problem is employed using a single frequency for 3D acoustic wave simulation (Hustedt et al., 2004). It is reduced from the 3D elastic wave field simulator developed by Petrov and Newman (2012). Most of the methods that have been developed for wave modeling in the frequency domain (see Lysmer and Drake (1972); Marfurt (1984); Pratt and Worthington (1990); Zahradník and Urban (1984); Jo et al. (1996); Štekl and Pratt (1998); Hustedt et al. (2004); Operto et al. (2007)) are based on solving the acoustic wave equation by the finite-difference method: on a uniform grid, the finite-difference methods provide an excellent compromise between accuracy and computational efficiency.

Governing Equations

We consider the first-order hyperbolic system in a velocity-pressure formulation in the Laplace-Fourier domain. Let the 3D isotropic acoustic medium with density ρ and incompressibility κ occupy the region Ω. The equations of motion inside Ω are given by:

$$s\rho v_x = \partial_x P,$$
$$s\rho v_y = \partial_y P,$$
$$s\rho v_z = \partial_z P,$$
$$sP = \kappa \left[\partial_x v_x + \partial_y v_y + \partial_z v_z \right] + sm, \tag{1}$$

where s is the complex number given by $\sigma + i\omega$, σ is the Laplace damping factor, ω is the angular frequency, and $i = \sqrt{-1}$. The velocities v_x, v_y and v_z are the velocity wavefield components, P is the acoustic pressure, m is seismic moment density tensor, and the symbols ∂_x, ∂_y, and ∂_z denote the partial differential operators $\frac{\partial}{\partial x}$, $\frac{\partial}{\partial y}$, and $\frac{\partial}{\partial z}$, respectively. The Laplace-Fourier equations of motion (equation 1) are obtained by transforming the time-domain system of equations (Virieux, 1986) using the following Laplace-Fourier transform:

$$g(s) = \int_0^\infty g(t)e^{-st}\, dt. \tag{2}$$

where $g(t)$ includes the functions $v_x(t)$, $v_y(t)$, $v_z(t)$, and $P(t)$.

For the numerical solution of equation 1, we used second and fourth order finite-difference schemes with 7 and 13 point stencils, respectively. This system of equations must be augmented with boundary conditions. In the case of infinite media, the non-reflecting condition for wavefield components is applied at the boundaries of region Ω. We used the perfectly matched layer (PML) boundary conditions (Hastings et al., 1996; Kim and Pasciak, 2010). However, at a free-surface boundary, one needs to incorporate the following boundary:

$$P = 0. \tag{3}$$

EMBEDDED BOUNDARY METHOD

Introduction

Special attention to the numerical treatment of the free-surface boundary for topography is deserved because it does not follow naturally from a Cartesian grid. For acoustic forward modeling, second-order finite-difference methods do not implicitly satisfy the free-surface condition as is the case with finiteelement methods. Accurately implementing the free-surface condition on an irregular interface is difficult due to the nonlocal nature of the finite-difference schemes. It implies that acoustic velocities above the free-surface are required to compute the pressure at or immediately below the surface (Fichtner, 2011).

In this paper, we describe an embedded boundary method for the three-dimensional acoustic wave equation with irregular free-surface boundary on a Cartesian grid. By computing pressure on either sides of the interface, we

can satisfy a zero acoustic pressure at the free surface, yielding superior results compared to conventional implementations that model topography as a staircase approximation. Bohlen and Saenger (2006) concluded that to model topography with a staircase method, more than 60 grid points per minimum wavelength are required in a second-order scheme to obtain acceptable results.

Theory

In simple topography settings, where the free surface is a flat plane that coincides with the top plane of the finite-difference grid, the free-surface boundary condition may be realized without staircasing error (Graves, 1996; Gottschammer and Olsen, 2001). However, when the free surface has a more complicated geometric structure, incorporating the free-surface boundary condition becomes more challenging because the finite-difference stencil will cross over the free surface as illustrated in Figure 1.
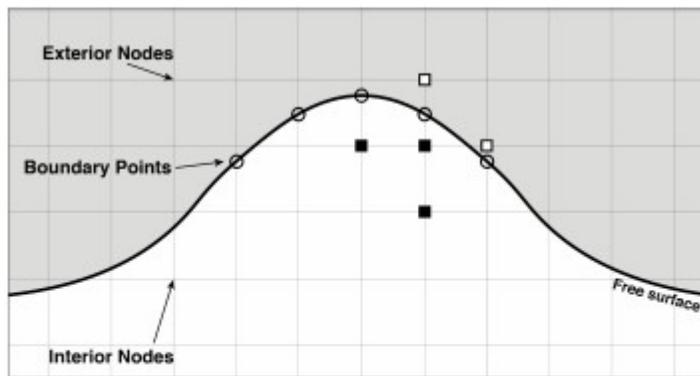

Figure 1: Smooth curved free surface on a uniform Cartesian grid for a second-order finite-difference stencil. *White squares* denote ghost nodes required by the stencil. *Black squares* denote the stencil interior grid nodes. *Circles* denote points on the free-surface that are *boundary* points.

We consider a case where the free surface is immersed within a regular finite-difference grid and assume a homogeneous media around the boundary. The free surface can be defined by the equation:

$$Z_S = f(x, y). \qquad (4)$$

We define grid nodes as *interior nodes* if they are inside the domain Ω and underneath the free-surface, as shown in Figure 1. Nodes outside the domain of interest, i.e., above the free surface, are defined as *exterior nodes*, and points on the free-surface boundary are defined as *boundary points*. The ghost nodes are defined to be grid points outside the domain of interest but still being requested by stencils. For example, the second-order finite-difference scheme with seven stencil points requires only one layer of nodes above the surface (Figure 1).

With the above definitions, the problem of free-surface boundary treatment becomes the problem of updating the wavefield at the ghost nodes such that the wavefield at boundary points is forced to be zero according to the boundary condition in equation 3. Because we know the exact values of the pressure at the boundary, the boundary condition may be realized as extrapolation or interpolation of the wavefield from the interior nodes to the ghost nodes via the boundary points.

The value of the pressure at the ghost nodes may be defined by the method of images (Jackson, 2007; Griffiths, 2005):

$$P_g = -P_{g,m}. \qquad (5)$$

For each ghost node P_g, we define a ghost mirror point $P_{g,m}$ inside the surface medium. For planar or spherical boundaries, the relationship ensures the boundary condition is exact (Morse and Feshbach, 1954). For an arbitrary boundary, it becomes an approximation. However, when the distance between the ghost node and the boundary is small (about one or two grid spacings), the boundary may be considered as locally planar. In this case, we can expect that equation 5 enforces equation 3 with good accuracy. Nodes above the ghost nodes that are not required by stencils are set to zero.

Ghost mirrors location

To locate the position of the ghost mirror, we find the closest distance between each ghost node at (x_g, y_g, z_g) and its interpolated surface $f(x, y)$. By considering the normal vector from the surface and the vector between the closest point on the surface and ghost node, we get the following system of non-linear equations:

$$\begin{cases} x - x_g + \partial_x f(x, y) \left[f(x, y) - z_g \right] &= 0 \\ y - y_g + \partial_y f(x, y) \left[f(x, y) - z_g \right] &= 0. \end{cases} \qquad (6)$$

By solving the system for x and y using the steepest-descent method, we attain the location of the closest point at the surface relative to the ghost node.

For a planar free surface, the distance ξ_R between P_g and the surface is equivalent to the distance ξ'_R between $P_{g,m}$ and the surface. However, if the surface is curved, the two distances (ξ_R and ξ'_R) are not equal (see Figure 2). Our algorithm accounts for curvature of the surface and corrects the location of the ghost mirror $P_{g,m}$ by assuming the free surface is spherical. Since we know the approximated topography f, we can find the mean radius for the curvature using:

$$R = \left| \frac{-2}{\nabla \cdot \hat{n}} \right|$$

$$= \left| \frac{2 \cdot \left(1 + (\partial_x f)^2 + (\partial_y f)^2\right)^{3/2}}{(1 + (\partial_x f)^2)\partial_{yy} f - 2\partial_x f \partial_y f \partial_{xy} f + (1 + (\partial_y f)^2)\partial_{xx} f} \right|, \tag{7}$$

where $\hat{n}$ is the normal to the local surface f (Spivak, 1981). Hence, ξ'_R can be found by:

$$\xi'_R = R(1 - \frac{R}{a}), \tag{8}$$

and the ghost node P_g is related to the ghost mirror $P_{g,m}$ by:

$$P_g = - \left(\frac{a}{R}\right) P_{g,m}, \tag{9}$$

where R is the radius of the curvature and a is the distance between the curvature origin and ghost node P_g. Assuming the surface is curved produces marginally better results compared to assuming a planar surface.

DISCONTINUOUS MESH METHOD

Theory

In typical seismic models, the velocity and density tends to increase with depth. Thus, small cell sizes can be used at the top and and larger cell sizes can be used at deeper regions of the model. This issue can be partly addressed by varying the vertical cell sizes (Δz) with depth. However, lateral cell sizes (Δx and Δy) are still constrained by the global minimum velocity (Pasalic et al., 2010).

We make x, y and z meshing to be discontinuous to take advantage of variations in velocity. Our approach divides the model into a number of regions, separated by horizontal planes (Figure 3). Within each region, Δx, Δy, and Δz are uniform and equal; however, they vary from region to region. In this way, discretization becomes a discontinuous function of depth.
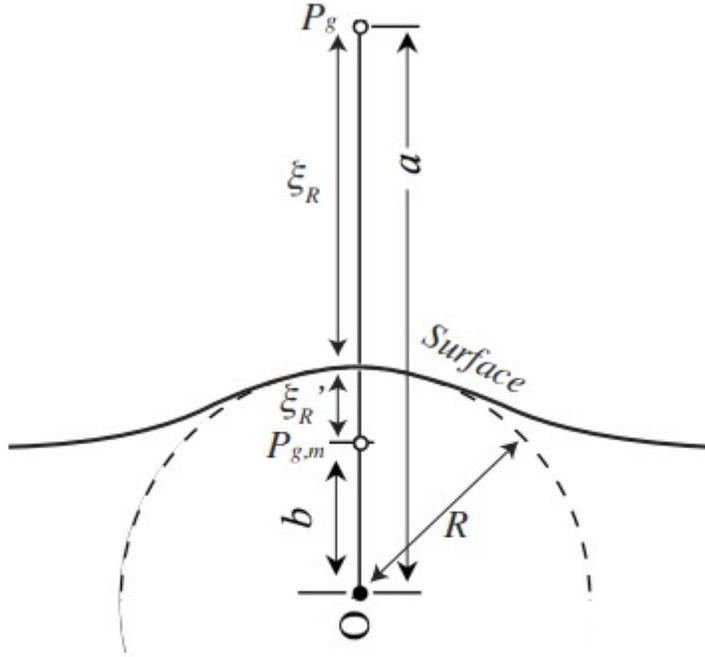
Figure 2: Method of images implementation: P_g denotes the location of the ghost node, $P_{g,m}$ denotes the updated location of the ghost mirror due to the curved surface, and R denotes the radius of the curvature.

Communication across region interfaces

Within each discontinuous region, the wave propagation calculations can be performed as for the uniform mesh. However, we clearly need to have some communication across the region interfaces (Figure 3). This can be done by simple trilinear interpolation across the relevant acoustic pressure values from one region to another. Hence, using finite difference, the wave propagation in Laplace-Fourier domain can be approximated by

$$
\begin{pmatrix}
A_1 & A_{1,2} & 0 & \cdots & & 0 \\
A_{2,1} & A_2 & A_{2,3} & \ddots & & \vdots \\
0 & \ddots & \ddots & \ddots & & 0 \\
\vdots & & \ddots & A_{n-1,n-2} & A_{n-1} & A_{n-1,n} \\
0 & \cdots & & 0 & A_{n,n-1} & A_n
\end{pmatrix}
\begin{pmatrix} P_1 \\ \vdots \\ \vdots \\ P_n \end{pmatrix}
=
\begin{pmatrix} F_1 \\ \vdots \\ \vdots \\ F_n \end{pmatrix}
\tag{10}
$$

where A_i is the forward modeling operator for region i, $A_{i,j}$ is the interpolation operator from region j to region i, and P_i and F_i are the acoustic pressure and source function for region i, respectively.

The proposed discontinuous mesh finite-difference scheme is a flexible technique which brings significant savings in computational effort and memory requirements. However, certain constraints must be observed. The most important constraint is the number of communication layers across the region interfaces. For an N-th-order-finite-difference scheme, the communication will occur over $2N$ layers (planes for 3-D case) in z-direction to ensure minumum reflection from the interface.
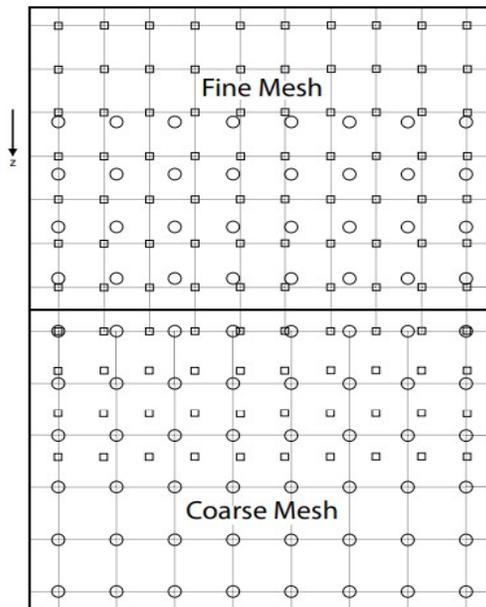

Figure 3: Communication between a fine and coarse mesh for second-order finite difference scheme. The interface is shown as a horizontal line.

NUMERICAL TESTS

Two experiments are performed to test the embedded boundary and discontinuous mesh methods on 3-D homogeneous velocity models. For the first experiment, we use second-order finite-difference embedded boundary scheme to test our embedded boundary method on the hill surface depicted in Figure 4. We compare a profile 50 m below the *central line* profile and implement a homogeneous media with velocity of 2250 m/s, density of 2300 kg/m³, and uniform grid spacing of 50 m. The source is the Ricker-wavelet with a frequency of 2 Hz and damping $1\frac{1}{s}$ and is located at $(x, y, z) = (1200, 1200, 2600)$ m. For this experiment, spacing has been reduced for the staircase solution to demonstrate that when spacing is reduced for the staircase method, the higher resolution solution converges to the embedded boundary method solution with spacing 50 m (Figure 5).

The second experiment is performed on homogeneous velocity model, with a velocity of 5000 *m/s*. The excitation is applied 20 *m* below and normal to the 10° sloping free-surface. Mesh spacing discontinuously increases with depth

in such a way as to ensure a minimum of 10 points per shortest wavelength.

A Ricker wavelet with a frequency of 20 Hz and damping $1\frac{1}{s}$ is used as the source waveform. Observation points are placed 5 m below and normal to the sloping free-surface. The situation is depicted in Figure 6.

In the experiment, the discontinuous mesh with embedded boundary method is applied on a second-order finite-difference scheme to calculate the pressure response at observation points. The acoustic pressure values corresponding to observation points are shown in Figure 7. The acoustic pressure values obtained by the analytical solution and discontinuous mesh with embedded boundary are compared. Overall, the mean error for the method is less than 5% (Figure 8).
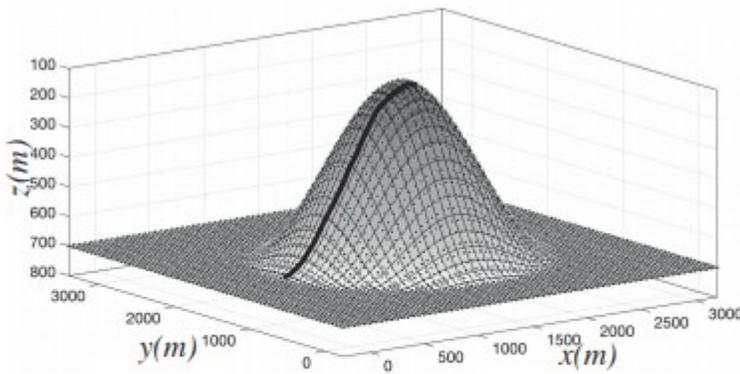

Figure 4: Hill topography with *black line* denoting central line profile. The grid spacing is 50 m in all three components and the source is located at $(x, y, z) = (1200, 1200, 2600)$m.
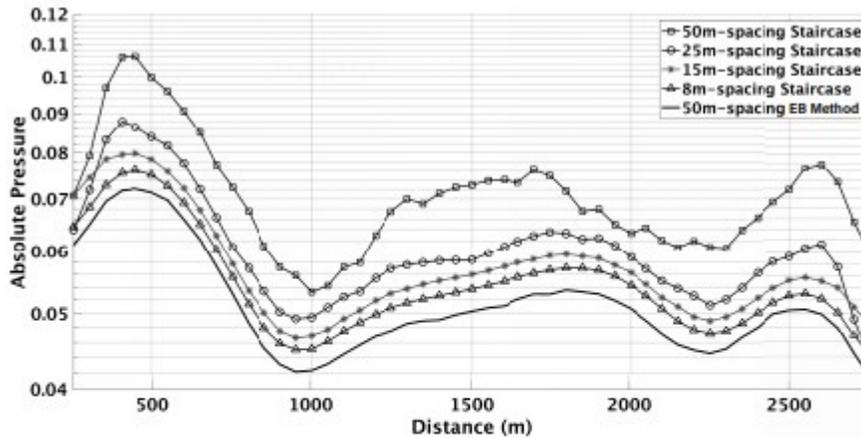
Figure 5: Absolute pressure solutions for *second-order* finite-difference scheme staircase with different cell sizes and embedded boundary methods for the hill model *central line* at 50 m below the surface.

CONCLUSIONS

We presented a discontinuous mesh with embedded boundary finite-difference scheme for solution of the Laplace-Fourier acoustic wave equation. Our embedded boundary method uses a regular Cartesian grid system, which greatly simplifies mesh generation and omits the need to change our current finite-difference formalizations. The free-surface boundary is enforced at actual surface locations through the method of images, allowing for an accurate representation of an arbitrary free-surface geometry. The discontinuous mesh method is ideal for use in acoustic modeling with topography and full waveform inversion since it leads to considerable savings in both computation time and memory requirements. These savings are primarily due to a reduction in the total number of finite-difference cells.
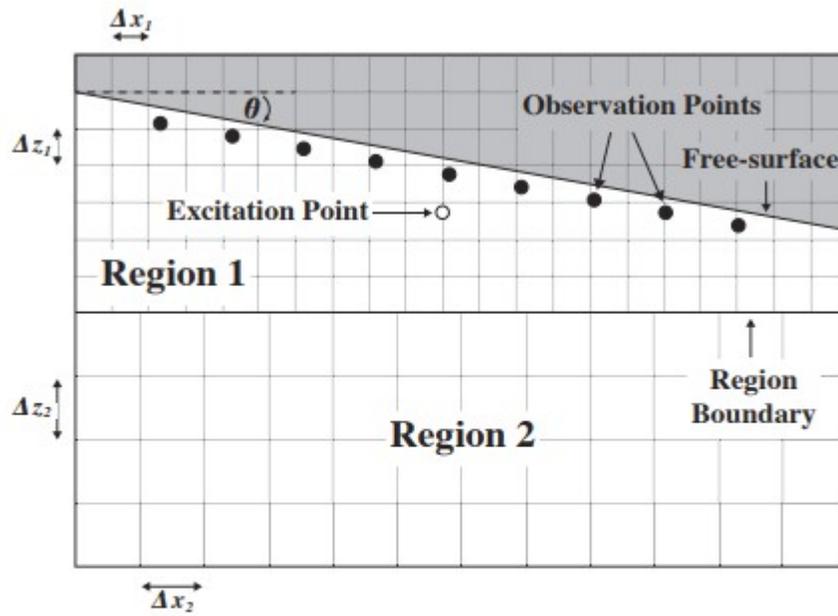
Figure 6: Mesh consisting of a sloping free-surface and two discontinuous regions. The near-surface observation points are used for calculation of error caused by the embedded boundary and discontinuous mesh methods for a homogeneous model.
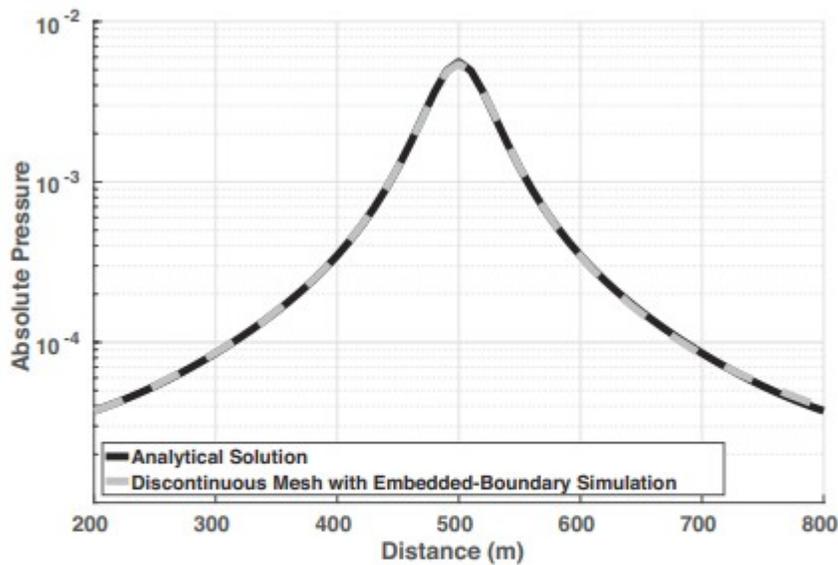
Figure 7: Absolute pressure for second-order finite-difference scheme at the observation points in Figure 6. The plot demonstrates the solution for a frequency of 20 Hz with damping $1\frac{1}{s}$ relative to the analytical solution.
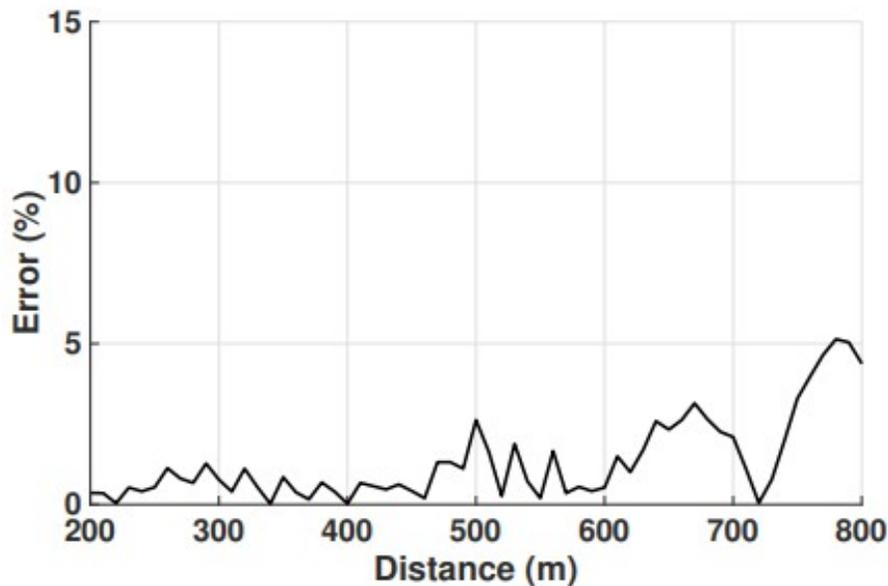

Figure 8: Error for second-order finite-difference scheme embedded boundary with discontinuous mesh relative to the analytical solution.

REFERENCES

Bohlen, T., and E. H. Saenger, 2006, Accuracy of heterogeneous staggered-grid finite-difference modeling of Rayleigh waves: Geophysics, 71, no. 4, T109–T115, https://doi.org/10.1190/1.2213051.

Fichtner, A., 2011, Full seismic waveform modelling and in-version: Springer.

Gottschammer, E., and K. Olsen, 2001, Accuracy of the explicit planar free-surface boundary condition implemented in a fourth-order staggered-grid velocity-stress finite-difference scheme: Bulletin of the Seismological Society of America, 91, 617–623, https://doi.org/10.1785/0120000244.

Graves, R. W., 1996, Simulating seismic wave propagation in 3d elastic media using staggered-grid finite differences: Bulletin of the Seismological Society of America, 86, 1091–1106.

Griffiths, D. J., 2005, Introduction to electrodynamics: AAPT.

Hastings, F. D., J. B. Schneider, and S. L. Broschat, 1996, Application of the perfectly matched layer (PML) absorbing boundary condition to elastic wave propagation: The Journal of the Acoustical Society of America, 100, 3061–3069, https://doi.org/10.1121/1.417118.

Hustedt, B., S. Operto, and J. Virieux, 2004, Mixed-grid and staggered-grid finite-difference methods for frequency- domain acoustic wave modelling: Geophysical Journal International, 157, 1269–1296, https://doi.org/10.1111/j.1365-246X.2004.02289.x.

Jackson, J. D., 2007, Classical electrodynamics: John Wiley & Sons.

Jo, C. -H., C. Shin, and J. H. Suh, 1996, An optimal 9-point, finite-difference, frequency-space, 2-D scalar wave extrapolator: Geophysics, 61, 529–537, https://doi.org/10.1190/1.1443979.

Kim, S., and J. E. Pasciak, 2010, Analysis of a Cartesian PML approximation to acoustic scattering problems in R2 : Journal of Mathematical Analysis and Applications, 370, 168–186, https://doi.org/10.1016/j.jmaa.2010.05.006.

Lysmer, J., and L. A. Drake, 1972, A finite element method for seismology: Methods in Computational Physics, 11, 181–216.

Marfurt, K. J., 1984, Accuracy of finite-difference and finite-element modeling of the scalar and elastic wave equations: Geophysics, 49, 533–549, https://doi.org/10.1190/1.1441689.

Morse, P. M., and H. Feshbach, 1954, Methods of theoretical physics: AAPT.

Operto, S., J. Virieux, P. Amestoy, J. -Y. L'Excellent, L. Giraud, and H. B. H. Ali, 2007, 3D finite-difference frequency-domain modeling of visco-acoustic wave propagation using a massively parallel direct solver: A feasibility study: Geophysics, 72, no. 5, SM195–SM211.

Pasalic, D., and R. McGarry, 2010, A discontinuous mesh finite difference scheme for acoustic wave equations: 80th Annual International Meeting SEG, Expanded Abstracts, SEG, 2940–2944, https://doi.org/10.1190/1.3513457.

Petrov, P. V., and G. A. Newman, 2012, 3D finite-difference modeling of elastic wave propagation in the Laplace-Fourier domain: Geophysics, 77, no. 4, T137–T155, https://doi.org/10.1190/geo2011-0238.1.

Pratt, R. G., and M. Worthington, 1990, Inverse theory applied to multi-source cross-hole tomography. Part 1: Acoustic wave-equation method: Geophysical Prospecting, 38, 287–310, https://doi.org/10.1111/j.1365-2478.1990.tb01846.x.

Spivak, M., 1981, Comprehensive introduction to differential geometry. Vol. 4: Publish or Perish, Inc., University of Tokyo Press.

Štekl, I., and R. G. Pratt, 1998, Accurate viscoelastic modeling by frequency-domain finite differences using rotated operators: Geophysics, 63, 1779–1794, https://doi.org/10.1190/1.1444472.

Virieux, J., 1986, P-SV wave propagation in heterogeneous media: Velocity-stress finite-difference method: Geophysics, 51, 889–901, https://doi.org/10.1190/1.1442147.

Zahradník, J., and L. Urban, 1984, Effect of a simple mountain range on underground seismic motion: Geophysical Journal International, 79, 167–183.